

## Investigating empirical models to retrieve the backscattering slope from Landsat 8 Images - The case of Lago Grande Curuai

Lino Augusto Sander De Carvalho<sup>1,2</sup>  
Vitor Souza Martins<sup>1,2</sup>  
Felipe de Lucia Lobo<sup>1,2</sup>  
Claudio Clemente Faria Barbosa<sup>1</sup>  
Evelyn Márcia Leão de Moraes Novo<sup>2</sup>

<sup>1</sup> Divisão de Processamento de Imagens - DPI

<sup>2</sup> Divisão de Sensoriamento Remoto - DSR

Instituto Nacional de Pesquisas Espaciais – INPE

Caixa Postal 515 – 12245-970 – São José dos Campos - SP, Brasil

lino.sander, vitor.s.martins1, felipellobo@gmail.com; claudio.barbosa, evlyn@inpe.br

**Abstract.** This paper aims on the investigation of well-established models to retrieve the backscattering slope ( $\gamma_{b_{bp}}$ ) from remote sensing images applied to a particular Amazon floodplain lake, named Curuai Lake. Lee, Carder e Arnone (2002)  $\gamma_{b_{bp}}$  model and its derivation, Pan et al. (2015) model, were applied to measured Remote Sensing Reflectance and retrieved  $\gamma_{b_{bp}}$  was compared to measured  $\gamma_{b_{bp}}$  taken in two distinct hydrological periods: receding and rising water periods (August 2013 and April 2014). Also, an empirical model, based on Lee, Carder e Arnone (2002) approach, was derived from a nonlinear fitting to the measured dataset, considering only Landsat 8 bands combination. Lee, Carder e Arnone (2002) and Pan et al. (2015) models were not suitable to retrieve backscattering slope in Curuai Lake whilst the empirical model using bands  $B_4(655)/B_5(865)$  presented the best result considering both hydrological periods and was therefore applied to Landsat 8 images acquired in August 2013 and April 2014. The qualitative inspection of both images reveal consistent backscattering slope retrievals which, with further analysis, could lead to a suitable proxy for particle size in Curuai Lake.

**Keywords:** Inland Waters, Inherent Optical Properties, Backscattering Slope .

### 1. Introduction

Amazon floodplain lakes (AFL) have singular characteristics regarding suspended matter (SM) seasonality. Due to variable degrees of lake connectivity to the Amazon river (BONNET et al., 2008; RUDORFF; MELACK; BATES, 2014), SM exchange process between river and lakes (river/lake inflow during rising water period and lake/river outflow during receding water period) controls the load and grain size distribution to the different lakes, what is strictly linked to biogeochemical process (LEITE et al., 2011). To enable synoptic and temporal analysis of floodplain lakes SM distribution in the Amazon basin, a series of remote sensing algorithms have been tested with relatively success (MONTANHER et al., 2014; LOBO; COSTA; NOVO, 2014). Particularly, the “Nechad algorithm” (NECHAD; RUDDICK; PARK, 2010) tested at the Curuai lake (Sander de Carvalho, 2016) proved to be useful for retrieving SM load for a complete hydrological cycle of the AFL.

However, to better understand SM type, further information is needed. Particle attenuation ( $c_p$ ), scattering ( $b_p$ ) and backscattering ( $b_{bp}$ ) coefficients are generally represented by a power law (CLAVANO; BOSS; KARP-BOSS, 2007). It has been shown that the slope of coefficients power law ( $\gamma_c, \gamma_{b_p}, \gamma_{b_{bp}}$ ) are theoretically and empirically related to the slope of a particle size distribution (PSD) represented by a Junge distribution ( $\xi$ ) (SLADE; BOSS, 2015). The simple relation  $\gamma_x = \xi - 3$ , with  $x = c_p, b_p, b_{bp}$ , however, still needs further validation, specially in Amazon turbid waters, but, represents a potentiality on particle size retrievals based on remote

sensing images.

Remote sensing algorithms have been currently tested to retrieve the slope of backscattering distribution ( $\gamma_{b_{bp}}$ ) but, particularly, the QAA algorithm (LEE; CARDER; ARNONE, 2002), which is widely used for Case I and recently adapted for Case II waters (MISHRA; MISHRA; LEE, 2014), uses an empirical approach to retrieve  $\gamma_{b_{bp}}$ . This retrieval is mainly based on empirical data and demands site specific testing. In the present study, Lee 2002  $\gamma_{b_{bp}}$  model is applied to a dataset acquired in two distinct hydrological phases at Curuai Lake (receding water period - August 2013 and rising water period - April 2014) to assess model's accuracy. In order to develop a local set of coefficients for  $\gamma_{b_{bp}}$  retrieval from OLI/Landsat 8 images, Lee 2002  $\gamma_{b_{bp}}$  model was fitted to measured  $R_{rs}$  and  $\gamma_{b_{bp}}$  derived from measured  $b_{bp}$ . It is also a goal of this study to find a model applicable to all phases of the hydrological year and therefore the best global model as well as Nechad algorithm was later applied to the OLI images acquired for both hydrological phases, in order to investigate  $\gamma_{b_{bp}}$  model results.

## 2. Study Area

The Lago Grande de Curuai (LGC) floodplain is located on the southern margin of the Amazon River, near Óbidos city (Brazil), 900 km upstream from the Atlantic Ocean. It is a complex system of about 30 shallow interconnected lakes with spatially and temporally variable hydraulic connectivity among themselves and with the Amazon River. As described by Barbosa et al. (2009), the effect of the seasonal flood pulse coupled with alluvial landforms, leads to complex water flow and mixing patterns in the Curuai floodplain lake system. The lake's stage is commonly divided in four periods: *Rising*, *High*, *Receding* and *Low* water periods and particularly, in the rising water period there is an inflow from the Amazon River which brings inorganic sediments which mostly enters the floodplain as diffuse *overbank flow*. On the other hand, during the receding water period, the lake is sufficiently shallow for fine deposited sediments to be resuspended by wind, resulting in high values and variability of suspended sediment and chlorophyll-a concentrations (BONNET et al., 2008; RUDORFF; MELACK; BATES, 2014).

### 2.1. Dataset

Dataset was collected in two field campaigns that took place in *August* (2013) and *April* (2014) (Hereafter called *August* and *April* for brevity). Scattering ( $b$ ) and backscattering coefficients ( $b_b$ ) as well as above water remote sensing reflectance ( $R_{rs}$ ) measuring procedures will be shortly described. A fully description of dataset, measuring procedures and sampling locations are presented in Sander de Carvalho (2016).

### 2.2. Scattering and Backscattering Measurements

The particulate scattering ( $b_p$ ) and backscattering ( $b_{bp}$ ) coefficients were measured with an optical package containing a 10 cm WetLabs ACS, a HOBILabs HydroScat-6 and a SeaBird SBE-37SI CTD throughout concurrent profiles of the absorption ( $a$ ) and attenuation ( $c$ ) coefficients, the backscattering coefficient, temperature and pressure respectively. At each station, the optical package was lowered to allow for instrument acclimation and warm up period (6 to 8 min) and to help remove air bubbles. Due to constraints imposed by the frame supporting the optical package, ACS intakes were at a minimum depth of 0.4 to 0.5 meters and hence no data is available closer to the surface. Details of equipments quality assessment and control are presented in Sander de Carvalho (2016). Optical package profiles were binned using a 10 cm median window and ACS measurements and temperature corrected. For the scattering correction for the ACS absorption tube the correction proposed by Röttgers, McKee e Wozniak (2013) was chosen (Sander de Carvalho, 2016). The scattering coefficient was calculated as  $b = c -$

a. For  $b_b$  measurements the processing scheme followed Sander de Carvalho et al. (2015) with a particularity on the *sigma* correction where the sigma factor ( $K_{bb}$ ) assumed a lower value than the proposed in HobiLabs User's Manual (2010) (Sander de Carvalho, 2016).

### 2.3. Slope of $b_p$ and $b_{bp}$ ( $\gamma_{b_p}$ and $\gamma_{b_{bp}}$ )

A median (and standard deviation) of  $b_p$  and  $b_{bp}$  measurements was taken from 0.5 to 1.0 meters since, ACS and Hydrosat-6 measurements are only available below 0.5 meters. The scattering and backscattering slopes were derived by fitting a power-law function (equation 1) of the particulate scattering and backscattering spectra using a non-linear fit.

$$x = x(\lambda_{ref}) \cdot \left( \frac{\lambda_{ref}}{\lambda} \right)^{\gamma_x} \quad (1)$$

Where  $x = b_p$  or  $b_{bp}$ ;  $\lambda$  is the wavelength and the reference wavelengths ( $\lambda_{ref}$ ) were chosen as 555 nm and 510 nm respectively (Sander de Carvalho, 2016).

### 2.4. $R_{rs}$ Measurements

Radiometric measurements were carried out with three intercalibrated TRIOS sensors (TRIOS, 2015). All measurements were carried out from 9:30 a.m. to 3:00 p.m. local time, avoiding large solar zenith angles. The Water Leaving Radiance ( $L_T$ ) measurements were carried out with a sensor-viewing geometry of  $45^\circ$  zenith angle and approximately  $137^\circ$  azimuth angle taking the Sun direction as reference (MOBLEY, 1999, 2015) ( $L_T(0^+, \theta \approx 45^\circ, \phi \approx 137^\circ, \lambda)$ ). To account for skylight surface reflection reaching the  $L_T$  sensor, a  $L_{sky}$  (Sky Radiance) measurement was taken in the same plane but with a rotation of the mounting pole  $\approx 45^\circ$  upward from nadir ( $L_{sky}(0^+, \theta \approx -45^\circ, \phi \approx 137^\circ, \lambda)$ ). The downwelling irradiance ( $E_s = E_d(0^+, \lambda)$ ) was measured on the top of the boat ( $\approx 5$ m) to avoid any interference. Sun/Skyglint effects were corrected by Mobley (1999) methodology, but taking  $\rho_{sky}$  factor from Mobley (2015). The in-water remote sensing reflectance ( $R_{rs}(0^-)$ ) was calculated from the above water remote sensing reflectance ( $R_{rs}(0^+) = \frac{L_T - L_{sky}}{E_s}$ ) following Sander de Carvalho (2016).

### 2.5. Landsat 8 Atmospheric Correction

Two Landsat 8 images acquired in August 2013 and April 2014 (Level 1T) were downloaded from USGS portal (USGS, 2016) and processed using the ACOLITE software (ACOLITE, 2016) (VANHELLEMONT; RUDDICK, 2015). The following steps were followed to achieve  $R_{rs}$  from images: (1) *per pixel* epsilon based on SWIR (bands 6 (1609 nm) and 7 (2201 nm)); (2) Pathlevan R Gains; (3) No resampling; (4) Cloud masking with a threshold equals to 0.03 using band as masking.

#### 2.5.1. Backscattering Model retrieval from remote sensing

Lee 2002  $\gamma_{b_{bp}}$  model was applied to retrieve the backscattering slope from remote sensing. The model, an empirical step of the QAA algorithm uses the following expression:

$$Y = 2.2 \left\{ 1 - 1.2 \cdot \exp \left[ -0.9 \cdot \frac{R_{rs}(0^-(440))}{R_{rs}(0^-(555))} \right] \right\} \quad (2)$$

where  $Y = \gamma_{b_{bp}}$ . Two other approaches were also tested: i) Pan et al. (2015) approach which uses a different version of Lee 2002  $\gamma_{b_{bp}}$  model based in distinct  $R_{rs}(0^-)$  bands (560 and 750 nm); ii) a non-linear fitting, performed using measured  $\gamma_{b_{bp}}$  and  $R_{rs}(0^-)$  for the following

combination of Landsat 8 bands :  $B_1(443)/B_2(483)$ ;  $B_2(483)/B_3(561)$ ;  $B_3(561)/B_4(655)$ ;  $B_4(655)/B_5(865)$ . Tests were performed using both individual (Apr and Aug) and coupled (Aug/Apr) datasets.

### 3. Results and Discussion

#### 3.1. Backscattering Retrieval Model

The  $\gamma_{b_p}$  and  $\gamma_{b_{bp}}$  comparison is presented in Figure 1. Although the range of both,  $\gamma_{b_p}$  and  $\gamma_{b_{bp}}$  are within the expected range it does not present a linear relationship. Also, for some samples, the standard deviation spans over the expected range, which increase the level of uncertainty. According to the literature (SLADE; BOSS, 2015),  $\gamma_{b_p}$  and  $\gamma_{b_{bp}}$  were found to linearly correlate and reasons for lack of correlation in this study could be explained by equipment characteristics, which require a set of corrections due to optical active components (OAC) ranges and, sampling characteristics, which requires high temporal and spatial resolution to capture the water column variability, particularly close to the surface (Sander de Carvalho, 2016).

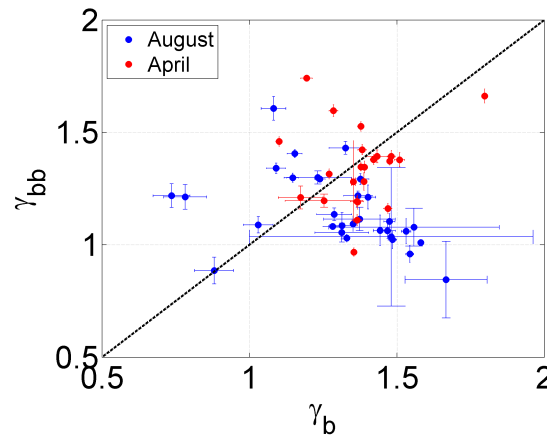


Figure 1:  $\gamma_{b_p}$  and  $\gamma_{b_{bp}}$  comparison - Dots represent the median from 0.5 to 1.0 meters depth. Bars represent the standard deviation. Color code: Blue-August 2013; Red - April 2014

Table 1 presents the Modular Relative Percent Difference (MRPD) (Sander de Carvalho, 2016) comparing Lee 2002 and Pan 2015  $\gamma_{b_{bp}}$  models to the nonlinear fitted models. All combinations of bands (wavelength centers) clearly outperforms Lee 2002 and Pan 2015 models, except for bands  $B_2(483)/B_3(561)$  whereas no fitting was achieved. The best models were achieved based only on data from August ( $B_3(561)/B_4(655)$ ) and April ( $B_4(655)/B_5(865)$ ). However as it is also a goal of this study to achieve a global model that could be applied to both August and April, the  $B_4(655)/B_5(865)$  model was chosen to be applied to Landsat 8 images.

Table 1: Modular Relative Percent Difference - MRPD for Modeled and Measured  $\gamma_{b_{bp}}$

	Lee 2002	Pan 2015	$B_1(443)/B_2(483)$	$B_2(483)/B_3(561)$	$B_3(561)/B_4(655)$	$B_4(655)/B_5(865)$
Aug/Apr	70.703	68.960	12.818 (%)	-	11.104 (%)	10.361 (%)
Aug	71.338	78.541	9.337 (%)	-	9.416 (%)	5.805 (%)
Apr	69.848	56.046	10.327 (%)	-	7.676 (%)	9.532 (%)

The same results presented in Table 1 are better observed in Figure 2.  $B_4(655)/B_5(865)$  (Aug/Apr) model is compared to Lee 2002 and Pan 2015 plotted with  $R_{rs}(0^-)$  and modeled  $b_b$  relation (Figure 2a). It is clear that Lee 2002 and Pan 2015 are not suitable to retrieve  $\gamma_{b_{bp}}$ . Figure 2b reinforce the suitability of the fitted model.

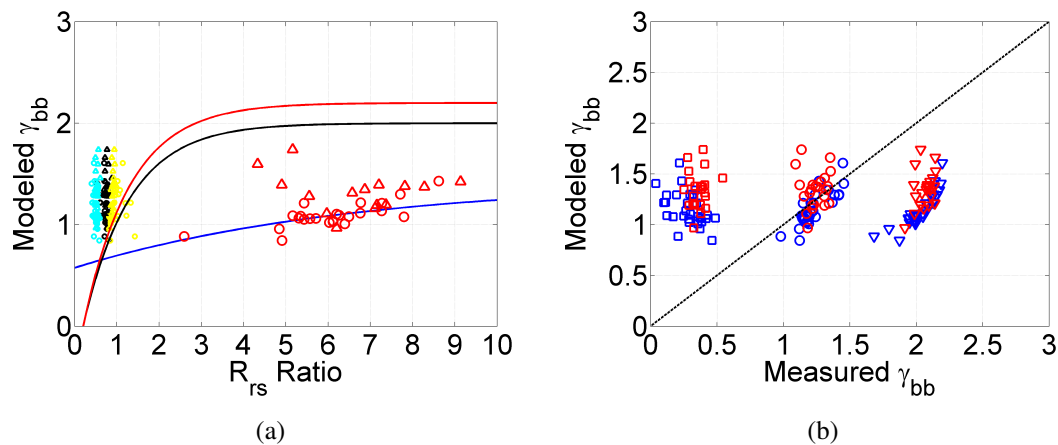


Figure 2: (a) Symbol Code - Circles: Samples from August; Triangles: Samples from April; Color Code - Cyan:  $B_1(443)/B_2(483)$ ; Black:  $B_2(483)/B_3(561)$ ; Yellow:  $B_3(561)/B_4(655)$ ; Red:  $B_4(655)/B_5(865)$ ; Line Code - Red: Lee 2002 model; Black: Pan 2015 model; Blue:  $B_4(655)/B_5(865)$  (Aug/Apr) model. (b) Color Code - Blue: August; Red: April; Symbol Code - Circles:  $B_4(655)/B_5(865)$  (Aug/Apr) model; Square: Pan 2015 model; Triangles: Lee 2002 model;

### 3.2. Application to Landsat 8 Images

In order to investigate the proposed  $\gamma_{b_{bp}}$  model,  $B_4(655)/B_5(865)$  (Aug/Apr) was applied to August 2013 and April 2014 Landsat 8 images. The  $B_4(655)/B_5(865)$  (Aug/Apr) was chosen since it presented the lowest MRPD among the tested for both August and April field campaigns. Figure 3 presents a comparison of a Landsat 8 Image from April 2014 RGB True Color (432),  $\gamma_{b_{bp}}$  model and Nechad model applied to Landsat 8 ( $B_4(655)$ ). April field campaign was carried out during Curuai Lake *rising period*, where water from the Amazon river drills into Curuai Lake from its western channels (figure 3a/b/c) and due to *overbank flow* (figure 3d/e/f). The black dashed circle highlights both phenomena and its is a particular example to qualitatively validate  $\gamma_{b_{bp}}$  model. From figure 3a it is possible to see a sediment plume entering Curuai Lake through west channels which increase sediment load and that is also confirmed by the SM concentration estimated by Nechad image in figure 3c. A similar behavior is observed in figure 3d in which, due to overbank flow, sediment load increases in the highlighted area (figure 3f). In both regions the  $B_4(655)/B_5(865)$  (Aug/Apr)  $\gamma_{b_{bp}}$  model indicates a lower  $\gamma_{b_{bp}}$  for the “highest sediment load area” when compared to different areas inside the lake.

Although it is not possible to direct relate  $\gamma_{b_{bp}}$  to particle size distribution,  $\gamma_{b_{bp}}$  model is a proxy for particle size variability. It is necessary, however, to prove that the effects observed in  $B_4(655)/B_5(865)$  (Aug/Apr)  $\gamma_{b_{bp}}$  derived images are not just an effect of higher reflectance due to higher sediment load. Inside the black dashed highlighted region, there is an inverse behavior in which a higher sediment load presented in Nechad images correspond to lower  $\gamma_{b_{bp}}$  in  $\gamma_{b_{bp}}$  image. If  $\gamma_{b_{bp}}$  could be related to particle size, that would indicate higher size particles entering Curuai Lake coming from the Amazon River. The red dashed highlighted region shows, on the other hand, a different target which indicates the same behavior as the black dashed region. From figure 3a it is possible to distinguish a phytoplankton bloom (*stripe* shape). Nechad image (figure 3c) shows a lower sediment load which agrees with a lower  $b_b$  from phytoplankton cells when compared to inorganic sediment. The  $\gamma_{b_{bp}}$  model from figure 3b also distinguishes the phytoplankton bloom showing lower  $\gamma_{b_{bp}}$ , which is consistent to the literature, in which  $\gamma_{b_{bp}}$  values are generally lower than inorganic sediment derived  $\gamma_{b_{bp}}$  (CLAVANO; BOSS; KARP-BOSS, 2007). Also, the lower  $\gamma_{b_{bp}}$  would indicate higher size particles which is consistent to a inorganic sediment/phytoplankton cell comparison.

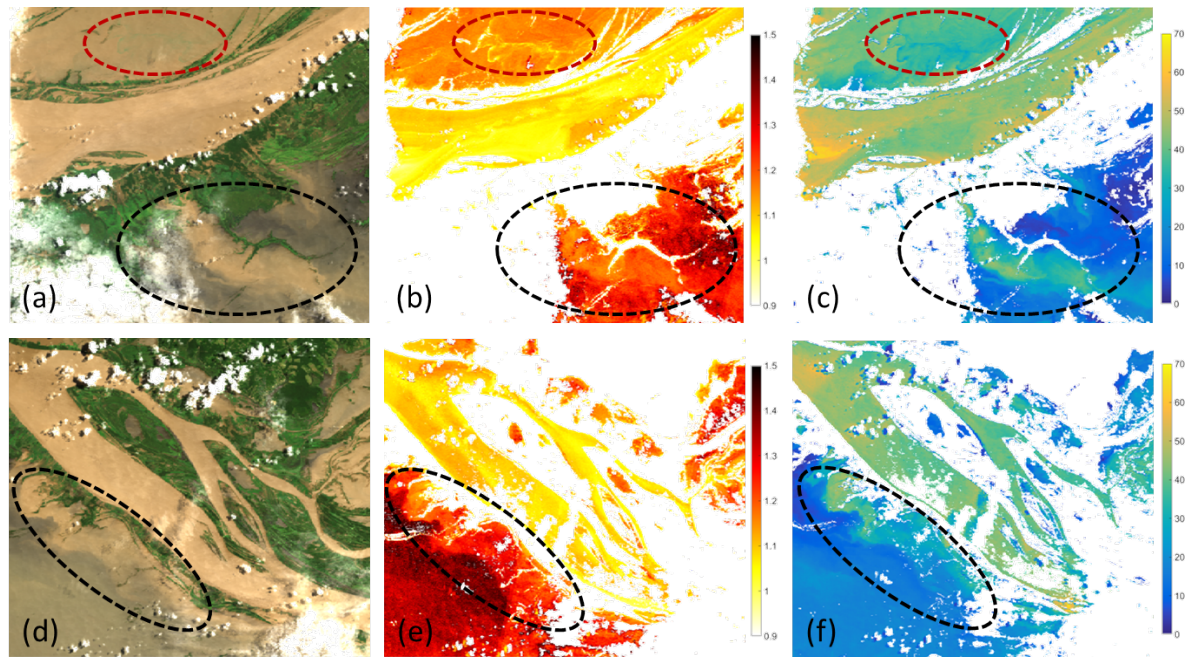


Figure 3: Landsat 8 Image (April 2014) - a/d RGB True Color (432) - b/e Aug/Apr  $B_4(655)/B_5(865)$   $\gamma_{bbp}$  model - c/f Nechad Model (Units of  $mg/L$ ).

Similarly to figure 3, figure 4 presents the comparison of a Landsat 8 Image from August 2013 RGB True Color (432) and to derived  $\gamma_{bbp}$  model and Nechad model. Different from April 2014, August 2013 field campaign was carried out during the Curuai Lake *receding period* in which the floodplain outflow exceeds Amazon river inflow. In this period, sediments are still mixed within the water column and chlorophyll-a concentration increases due to nutrient availability (BARBOSA et al., 2009), also increasing phytoplankton blooms. However, even in a Curuai's lake distinct hydrological conditions, results for  $\gamma_{bbp}$  model and the comparison to Nechad's images remain the same. Figure 4a shows a comparison of high sediment load area (black dashed line) and a phytoplankton bloom (red dashed line). Similar to April 2014, the Nechad image (figure 4c) indicates a higher sediment load for the black dashed highlighted area whereas for the phytoplankton bloom (red dashed highlighted area) a lower sediment load is presented. Figure 4b agrees with Nechad's image showing a lower  $\gamma_{bbp}$  for the phytoplankton bloom area when compared to  $\gamma_{bbp}$  in the sediment area. Figure 4d/e/f also reinforces the conclusions from figure 3. The variability in color (figure 4d),  $\gamma_{bbp}$  (figure 4e) and sediment load (figure 4f) follows the previous conclusions where a higher sediment load correspond to a lower  $\gamma_{bbp}$ .

#### 4. Conclusion

This study aimed on the investigation of well-established empirical models to retrieve  $\gamma_{bbp}$  from Remote Sensing images. The tested models from Lee 2002 and Pan 2015 did not lead to an accurate  $\gamma_{bbp}$  retrieval and were, both, outperformed by nonlinear fitted models. The combinations of August and April samples and bands  $B_4(655)/B_5(865)$  presented the best fitted model with a MRPD  $\approx 10\%$  error, which is a reasonable uncertainty for remote sensing based models. Landsat 8 images analysis apparently indicate consistency in  $\gamma_{bbp}$ , when confronted to Curuai Lake water dynamics but further analysis with a comprehensive dataset is necessary to derive a robust and accurate  $\gamma_{bbp}$  model which could also be related to particle size.

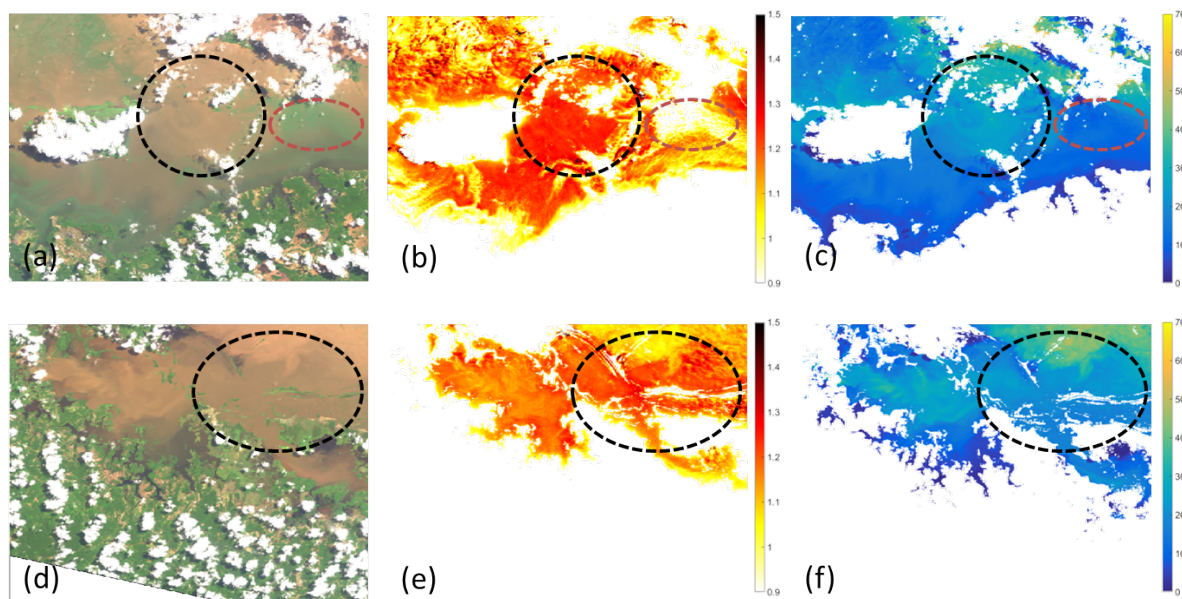


Figure 4: Landsat 8 Image (August 2013) - a/d RGB True Color (432) - b/e Aug/Apr  $B_4(655)/B_5(865) \gamma_{b_{bp}}$  model - c/f Nechad Model (Units of  $mg/L$ ).

## 5. Acknowledgements

The authors thank São Paulo Research Foundation (FAPESP) (Project 2011/23594-8 and 2016/09953-9), the Brazilian National Council for Scientific and Technological Development (CNPq) (Project 248457/2013-6), the Coordination for the Improvement of Higher Education Personnel (CAPES) for financial support and MSA-BNDES (1022114003005) for additional support.

## References

- ACOLITE. *ACOLITE*. 2016. Disponível em: <<http://odnature.naturalsciences.be/remsem/acolite-forum/>>.
- BARBOSA, C. C. F. et al. Geospatial analysis of spatiotemporal patterns of pH, total suspended sediment and chlorophyll-a on the Amazon floodplain. *Limnology*, v. 11, n. 2, p. 155–166, dec 2009. ISSN 1439-8621.
- BONNET, M. P. et al. Floodplain hydrology in an Amazon floodplain lake (Lago Grande de Curuai). *Journal of Hydrology*, v. 349, n. 2, p. 18–30, January 2008.
- CLAVANO, W. R.; BOSS, E.; KARP-BOSS, L. Inherent optical properties of non-spherical marine-like particles – from theory to observation. *Oceanography and Marine Biology: An Annual Review*, v. 45, p. 1–38, 2007.
- HYDRO-OPTICS, BIOLOGY AND INSTRUMENTATION LABORATORIES. *HydroScat-6 Spectral Backscattering Sensor & Fluorometer - user's manual: Revision j*. 12819 SE 38th St. 434 Bellevue, WA 98006 USA, 2010. 63 p.
- LEE, Z.; CARDER, K. L.; ARNONE, R. a. Deriving inherent optical properties from water color: a multiband quasi-analytical algorithm for optically deep waters. *Applied optics*, v. 41, n. 27, p. 5755–72, set. 2002. ISSN 0003-6935.
- LEITE, N. K. et al. Intra and interannual variability in the Madeira River water chemistry and sediment load. *Biogeochemistry*, v. 105, n. 1, p. 37–51, 2011. ISSN 01682563.

- LOBO, F. D. L.; COSTA, M. P. F.; NOVO, E. M. L. M. Time-series analysis of Landsat-MSS/TM/OLI images over Amazonian waters impacted by gold mining activities. *Remote Sensing of Environment*, Elsevier Inc., v. 157, p. 170–184, 2014. ISSN 00344257.
- MISHRA, S.; MISHRA, D. R.; LEE, Z. Bio-optical inversion in highly turbid and cyanobacteria-dominated waters. *IEEE Transactions on Geoscience and Remote Sensing*, v. 52, n. 1, p. 375–388, 2014. ISSN 01962892.
- MOBLEY, C. D. Estimation of the remote-sensing reflectance from above-surface measurements. *Applied Optics*, v. 38, n. 36, p. 7442–55, dec 1999. ISSN 0003-6935.
- MOBLEY, C. D. Polarized reflectance and transmittance properties of windblown sea surfaces. *Applied Optics*, v. 54, n. 15, p. 4828, may 2015. ISSN 0003-6935.
- MONTANHER, O. C. et al. Empirical models for estimating the suspended sediment concentration in Amazonian white water rivers using Landsat 5/TM. *International Journal of Applied Earth Observation and Geoinformation*, Elsevier B.V., v. 29, n. 1, p. 67–77, jun 2014. ISSN 03032434.
- NECHAD, B.; RUDDICK, K.; PARK, Y. Calibration and validation of a generic multisensor algorithm for mapping of total suspended matter in turbid waters. *Remote Sensing of Environment*, Elsevier Inc., v. 114, n. 4, p. 854–866, abr. 2010. ISSN 00344257.
- PAN, H. et al. An Improved Approach to Retrieve IOPs Based on a Quasi-Analytical Algorithm (QAA) for Turbid Eutrophic Inland Water. *IEEE Journal of Selected Topics in Applied Earth Observations and Remote Sensing*, v. 8, n. 11, p. 5177–5189, 2015. ISSN 21511535.
- RÖTTGERS, R.; MCKEE, D.; WOZNIAK, S. B. Evaluation of scatter corrections for ac-9 absorption measurements in coastal waters. *Methods in Oceanography*, Elsevier B.V., In press, p. 1–19, dez. 2013.
- RUDORFF, C. M.; MELACK, J. M.; BATES, P. D. Flooding dynamics on the lower Amazon floodplain: 2. Seasonal and interannual hydrological variability. *Water Resources Research*, v. 50, n. 1, p. 635–649, jan. 2014.
- Sander de Carvalho, L. A. *Bio-optical characterization of Amazon floodplain lakes and evaluation of the retrieval of optically active constituent using remote sensing*. 201 p. Tese (Doutorado) — Instituto Nacional de Pesquisas Espaciais (INPE), São José dos Campos, 2016-04-18 2016. Disponível em: <<http://urlib.net/sid.inpe.br/mtc-m21b/2016/06.08.16.27>>. Acesso em: 29 out. 2016.
- Sander de Carvalho, L. A. et al. Implications of scatter corrections for absorption measurements on optical closure of Amazon floodplain lakes using the Spectral Absorption and Attenuation Meter (AC-S-WETLabs). *Remote Sensing of Environment*, Elsevier Inc., v. 157, p. 123–137, feb 2015. ISSN 00344257.
- SLADE, W. H.; BOSS, E. Spectral attenuation and backscattering as indicators of average particle size. *Applied Optics*, v. 54, n. 24, p. 7264, ago. 2015. ISSN 0003-6935. Disponível em: <<https://www.osapublishing.org/abstract.cfm?URI=ao-54-24-7264>>.
- TRIOS. *Trios Sensors*. 2015. Disponível em: <<http://trios-science.com/>>.
- USGS. *Earth Explorer - USGS - United States Geological Service*. 2016. Disponível em: <<http://earthexplorer.usgs.gov/>>.
- VANHELLEMONT, Q.; RUDDICK, K. G. Advantages of high quality SWIR bands for ocean colour processing: Examples from Landsat-8. *Remote Sensing of Environment*, Elsevier B.V., v. 161, p. 89–106, 2015. ISSN 00344257.